



Few-layered MoS₂ vertically aligned on 3D interconnected porous carbon nanosheets for hydrogen evolution



Dongjin Ko^{a,1}, Xuanzhen Jin^{a,b,1}, Kwang-dong Seong^a, Bingyi Yan^a, Hua Chai^c, Jong Min Kim^a, Minsik Hwang^a, Juhyung Choi^a, Wang Zhang^{a,c,*}, Yuanzhe Piao^{a,d,*}

^a Graduate School of Convergence Science and Technology, Seoul National University, 145 Gwanggyo-ro, Yeongtong-gu, Suwon-si 16229, Gyeonggi-do, Republic of Korea

^b Department of Chemical Engineering and Technology, Yanbian University, Yanji 133002, Jilin, PR China

^c School of Chemistry and Chemical Engineering, Yangzhou University, Yangzhou 225002, Jiangsu, PR China

^d Advanced Institutes of Convergence Technology 145 Gwanggyo-ro, Yeongtong-gu, Suwon-si 16229, Gyeonggi-do, Republic of Korea

ARTICLE INFO

Keywords:

Interconnected porous carbon
MoS₂
Few-layered
Vertical alignment
Hydrogen evolution reaction

ABSTRACT

MoS₂ has been considered as a non-precious alternative to platinum based electrocatalyst for electrochemical hydrogen evolution. Since most of the active site exists on the edges of MoS₂, a material design that could increase the exposure of the edges could improve its catalytic activity. In this work, we prepared small sized and few-layered MoS₂ that is vertically aligned on three-dimensional interconnected porous carbon nanosheets (IPC). Benefiting from exposure of MoS₂ edges, MoS₂/IPC composite exhibits a high catalytic activity (225 mA cm⁻² at -250 mV vs. RHE, and Tafel slope of 38 mV dec⁻¹) and maintains steady performance for several hours. Since the procedure to prepare MoS₂/IPC composites is scalable and cost-effective, our method of preparing few-layered MoS₂ on porous carbon shows great potential as a competitive electrocatalysts for HER.

1. Introduction

Hydrogen has been considered to be a clean energy carrier towards the future. Unfortunately, hydrogen is mainly produced via reforming fossil fuels resulting in major byproducts such as greenhouse gases [1–3]. Electrochemical water splitting powered by a renewable energy is an eco-friendly way to produce hydrogen without emission of greenhouse gas; however the costs in relation to production cost imposes severe limitation to practical applicability. For hydrogen evolution reaction (HER), which occurs at the cathode part of the electrochemical water splitting cell, rare and expensive Platinum (Pt) based noble-metal electrocatalysts exhibits the best performance up to date. To be practical for industrial use, developing a low cost and high performing cost efficient electrocatalyst with high performance that can replace Pt-based material in production is essential [4–11].

Among the economical materials that have been investigated as Pt replacements for HER catalysis, MoS₂ shows promising results in regards to low cost [12], electrochemical stability [13], and high theoretical catalytic activity [14–20]. As of now, there are two major hindering factors in relation to catalytic performance of MoS₂: First, MoS₂ has a small number of active sites since the thermodynamically favored basal plane is catalytically inert [21,22]. In addition, terminal sulfide

groups at the edges of the MoS₂ layers has been regarded as catalytically active sites for HER. Second, MoS₂ has low electrical conductivity to supply the electrons to the active sites. [23–25] Therefore, synthesizing nanostructured MoS₂ nanosheets on conductive substrate could be an effective strategy to overcome the aforementioned obstacles.

Recently, significant efforts were made to prepare small sized MoS₂ with fewer layers [26–31]. Through this approach, the terminating sulfide groups at the edges of the MoS₂ can have maximum exposure and electrons can be easily transferred to the active edges by shortening the electron transport path. An alternative to improve the catalytic performance of MoS₂ is by preparing vertically aligned MoS₂ nanosheets on conductive support, which can increase the exposure of active edges [32–36]. Several groups demonstrated that the catalytic performance of vertically aligned MoS₂ nanosheets is much higher compared to randomly aligned MoS₂ nanosheets [32,33]. In addition, expanding interlayers of MoS₂ is an alternative strategy that can further enhance the catalytic activity of MoS₂. According to the theoretical studies, increasing the interlayer spacing of MoS₂ nanolayers can decrease hydrogen adsorption energy at the edges, which is favorable for catalyzing HER. Therefore, although preparing small sized and few-layered interlayer expanded MoS₂ nanosheets vertically aligned on conductive supports are quite challenging, it is the ideal way to enhance

* Corresponding authors.

E-mail addresses: zhangwang@yzu.edu.cn (W. Zhang), parkat9@snu.ac.kr (Y. Piao).

¹ D. Ko and X. Jin contributed equally to this work.

catalytic activity of MoS_2 .

Porous carbons had received remarkable attention due to their excellent electrochemical properties, low cost, and stability. Especially, high surface area of porous carbon has been used as a conductive support to immobilize nanosized material [37–39]. For MoS_2 , it is reported that the interaction between MoS_2 precursors and pores on carbon surface enables growth of highly dispersed MoS_2 nanoparticles [40,41]. As a reference, Liao et al. [41] used mesoporous graphene as both catalyst support and template to prepare MoS_2 nanodots. However, in these reports, the prepared few-layered MoS_2 nanosheets were horizontally positioned on porous carbon. As the active sites of MoS_2 nanosheets exist at the edges of the basal plane, horizontally supported MoS_2 nanosheet is not an effective design for exposing active edges.

In this paper, we prepared few-layered and vertically aligned MoS_2 by employing 3D interconnected porous carbon (IPC) with rich micro-, meso-, and macropores as conductive support. The micropores on the carbon surface play a role providing anchoring sites to deposit the few-layered MoS_2 nanosheets. As the composite material is composed of small-sized and few-layered MoS_2 nanosheets, $\text{MoS}_2/\text{IPC-2}$ exhibits high catalytic activity, which was comparable to most of MoS_2 /carbon electrocatalysts. The synthesis described in this paper is scalable and cost-effective; therefore, our method of preparing few-layered and vertically aligned MoS_2 is expected to be extended to a wide range of applications [42–44], including HER catalysts.

2. Experimental section

2.1. Synthesis of IPC

IPC was prepared through pyrolyzing potassium citrate under inert gas according to the method reported by Sevilla et al. [45]. Typical synthesis begins with grinding 3 g of potassium citrate with mortar to produce a fine powder. The precursor was thermally decomposed under Ar atmosphere up to 850 °C at a heating rate of 3 °C/min and held at that temperature for 2 h. After thermal treatment, the product was treated with hydrochloric acid to dissolve the remaining unreacted precursors. Next, the resultants were collected by centrifugation, followed by washing with water and ethanol three times. Finally, the products were lyophilized for several days to obtain fine powder. The obtained product was denoted as IPC.

2.2. Solvothermal synthesis of MoS_2/IPC composite

In a typical synthesis, 10 mg of IPC, and 20 mg of $(\text{NH}_4)_2\text{MoS}_4$ were dispersed in 10 mL of *N*, *N*-dimethylformamide (DMF) with the aid of ultrasonication for 30 min. After making a clear solution, it was transferred to 20 mL Teflon line autoclave and heated in an electrical oven at 200 °C for 10 h. The product ($\text{MoS}_2/\text{IPC-2}$) was washed several times with DI water and ethanol and dried overnight in 60 °C oven. In comparison, the weight ratio of IPC to $(\text{NH}_4)_2\text{MoS}_4$ varied from 1:1 and 1:4 while keeping the amount of IPC the same and denoted as $\text{MoS}_2/\text{IPC-1}$ and $\text{MoS}_2/\text{IPC-4}$, respectively. Bare MoS_2 was synthesized under a similar condition to $\text{MoS}_2/\text{IPC-2}$ without adding IPC.

2.3. Physical characterization

The morphology of the samples was analyzed using Hitachi S-4800 field emission scanning electron microscopy (FE-SEM). Samples were prepared by drop-casting a diluted suspension of a material in ethanol on an aluminum foil and electrically connected (Carbon tape) to an SEM stub. Transmission electron microscopy (TEM) and high-resolution transmission electron microscopy (HR-TEM) images were recorded using JEOL JEM-2010 operating at 300 kV. Samples were drop-casted from diluted ethanol dispersions of a material on a holey carbon coated 300 mesh Cu grids and dried using IR lamp. X-ray diffraction (XRD) patterns were tested by Bruker D8 advance superspeed powder

diffractometer with Cu K α radiation operating at 40 kV and 25 mA at a scan rate of 3° min $^{-1}$. Raman spectra were recorded by Renishaw Invia Raman spectroscopy equipped with a 514 nm excitation laser. The elemental composition of the catalysts was analyzed by using a wavelength dispersive X-ray Fluorescence (XRF) spectrometer II (Bruker, S8 TIGER).

X-ray photoelectron spectroscopy (XPS) were measured by Thermo Escalab 250 Xi system (Thermo Scientific) with a monochromated Al K α as the emission source at power of 150 W (14.9 kV \times 8.79 mA). The total pressure in the main vacuum chamber during analysis was approximately 9×10^{-9} mbar. Samples were filled into shallow wells of a custom-made sample holder and analyzed at an emission angle of 0° as measured from the surface normal. As the actual emission angle is ill-defined in the case of powders (ranging from 0–90°), the sampling depth may range from 0 to 10 nm. Binding energies were calibrated to the adventitious carbon C 1 s peak at 284.8 eV. XPS curve was fitted using Thermo Avantage software V5.978. The areas of the Mo 3d $_{3/2}$ and 3d $_{5/2}$ peaks were constrained to maintain a ratio of 2:3 during the fitting of the Mo 3d XPS spectra. For S 2p XPS spectra, the areas were constrained to ensure a proper 1:2 area ratio between the S 2p $_{1/2}$ and 2p $_{3/2}$ peaks.

Small angle X-ray scatter (SAXS) measurements have been performed on powder samples using a Nanostar U small-angle X-ray scattering system (Bruker, Germany) using Cu K α radiation (40 kV, 35 mA) with wavelength of 0.154 nm. Scattering of the samples was acquired in the range of $0.05 < q < 7 \text{ nm}^{-1}$. The formula $d = 2\pi/q$ was used to calculate the *d*-spacing values. Brunauer–Emmett–Teller (BET) analysis was carried out at –196 °C using ASAP 2020. Before the measurements, samples were dried at 100 °C for 4 h.

2.4. Electrochemical measurement

All electrochemical measurements were performed with a standard three-electrode setup that consists of Ag/AgCl filled with saturated KCl as a reference electrode, graphite rod as a counter electrode, and glassy carbon rotating disk electrode (RDE) modified with active materials as a working electrode. Before modifying the electrode, the glassy carbon surface was polished with 1.0 and 0.3 μm Al_2O_3 powders with a wet polishing pad. After polishing, remaining Al_2O_3 powders on the glassy carbon surface was thoroughly washed with water and sonicated in water for about 1 min. Additionally, RDE was rotated at 2400 rpm. Nitrogen saturated 0.5 M H_2SO_4 (pH 0.3) was used as an electrolyte.

5 mg of catalyst for testing was dispersed in a mixture of 440 μl of DI water, 440 μl of DMF, and 120 μl of Nafion (5 wt%, Aldrich) and ultrasonicated for 30 min to make a homogeneous slurry. Then, 10 μl of the catalyst containing slurry was drop-casted on glassy carbon electrode (GCE, diameter of 5 mm) with a loading mass of 0.254 mg cm^{-2} and dried using an infrared lamp.

All electrochemical measurements without Electrochemical Impedance Spectroscopy (EIS) analysis were held in Metrohm Autolab workstation PGSTAT 302 N. To add, the data was corrected to compensate iR losses during the measurements. The electrochemical catalytic activity of the catalysts was measured by using linear sweep voltammetry (LSV) with scan rate of 2 mV s $^{-1}$. To condition the electrodes, 30 cyclic voltammetry scans were conducted between 0 and -0.3 V (V vs. RHE) prior to LSV measurements. Double layer capacitance (related to the electrochemical surface of the catalyst) was measured at a potential range of 0.2 V to 0.3 V (V vs. RHE) by varying scan rate from 20 mV s $^{-1}$ to 70 mV s $^{-1}$ using CV. EIS was measured with electrochemical analyzer ZIVE SP1 with frequency ranging from 0.1 Hz to 10 6 Hz with an amplitude of 5 mV. To measure stability of the electrode, CV measurement was held in potential range of –0.3 to 0.2 V (V vs. RHE) with a scan rate of 50 mV s $^{-1}$. All measurement are measured respect to reversible hydrogen electrode according to following equation: E (V vs RHE) = E (V vs Ag/AgCl) + 0.197 + 0.0591 \times pH.

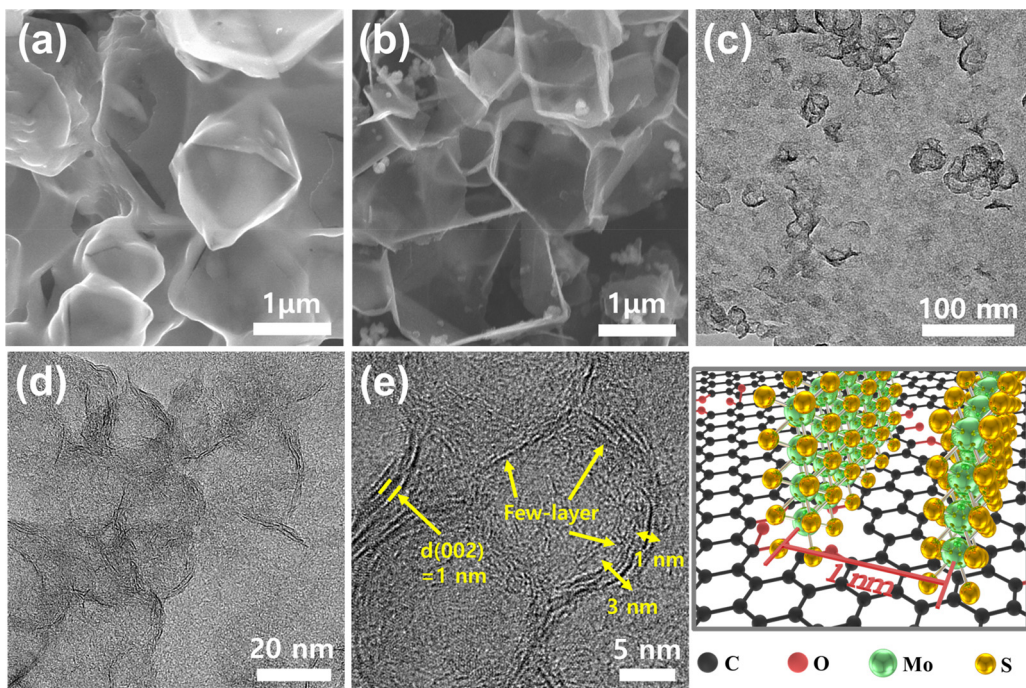


Fig. 1. SEM images of (a) IPC and (b) MoS₂/IPC-2; (c) Low- and (d, e) high-magnification TEM images and (f) XRD patterns of sample MoS₂/IPC-2.

3. Results and discussion

3.1. Synthesis and characterization of catalysts

The MoS₂/IPC composite was prepared via a two-step synthetic. The synthesis begins with preparation of IPC. IPC was prepared according to the method developed by Sevilla et al. [45] with slight modifications. Then, MoS₂ nanosheets were deposited on the IPC through solvothermal reducing (NH₄)₂MoS₄ in DMF. (NH₄)₂MoS₄ has been used as a source for both Mo and S. Since DMF has reducing ability under solvothermal condition, MoS₄²⁻ ions are reduced into MoS₂ [46].

Fig. 1 shows the morphologies of IPC and MoS₂/IPC composite formed from a 1:2 wt ratio of molybdenum sulfide precursor to IPC (MoS₂/IPC-2). As shown in Fig. 1a, IPC consists of several irregularly 3D interconnected nanosheets, with dimensions of several micrometers. Fig. 1b–e shows the SEM and TEM images of the MoS₂/IPC-2. It is observable that the morphology of the IPC is retained with nanometer sized few-layered MoS₂ grown on its surface. Morphology of MoS₂ synthesized without IPC support was flower-shaped, which confirms the role of IPC acting as a support material to form vertically aligned MoS₂ (Fig. S1). The HR-TEM image in Fig. 1e shows that MoS₂ layers are fewer than 3 layers while having interlayer distance (along the (002) direction) of ~1 nm, which is larger than the interlayer spacing of typical 2H-MoS₂ (0.615 nm). Meanwhile, large number of defects were observed in few-layered MoS₂ nanosheets.

The enlarged interlayer spacing of MoS₂/IPC-2 was also observed in X-ray diffraction (XRD) measurements. For MoS₂/IPC-2, diffraction peaks near 9.4° and 18.7°, which correspond to (002) and (004), are found (Fig. 2a). The highly symmetric diffraction peak at 9.4° reveals that MoS₂ layers are highly ordered along the c-axis. In reference to Bragg's law, the interlayer spacing along the (002) direction is determined to be approximately 1 nm, which is consistent with the value determined from the HR-TEM results. Since the solvothermal reaction is performed at a relatively short duration and low temperature of 200 °C, formation of defects in MoS₂ lattices are expected and is thought to be the cause of the interlayer expansion [47]. The number of layers was estimated by the Scherrer's equation from the (002) diffraction peak [48]. For bare MoS₂ and MoS₂/IPC-2 composite, the average number of

layers were estimated to be approximately, 4.61 nm and 3.23 nm, which is consistent to the TEM results (Fig. S1, Fig. 1e).

The chemical structure of the MoS₂/IPC composite is characterized by XPS (Fig. S3a). In Mo 3d spectrum of the MoS₂/IPC-2 (Fig. 3c), two characteristic peaks are located at 232.21 and 229.16 eV, which arises from Mo⁴⁺ 3d_{3/2} and Mo⁴⁺ 3d_{5/2}, respectively, are found. This result indicates that Mo⁴⁺ was dominant in MoS₂/IPC-2. In addition to Mo⁴⁺ state, peaks (236.01 eV, 232.96 eV, 233.31 eV, 229.96 eV) with high valence Mo states (Mo⁶⁺, Mo⁵⁺) are found (Fig. 3a, e). Since significant amount of high valence Mo states (Mo⁶⁺, Mo⁵⁺) are found, we think that molybdenum oxide in form of MoO_{3-x} or in molybdenum oxysulfide coexists with MoS₂ nanosheets according to result of previous studies. This form of molybdenum oxide is commonly observed when MoS₂ is slightly oxidized [49]. Fig. 3d shows the S 2p spectra of the MoS₂/IPC-2. In S 2p spectra, the peaks at 163.17 and 164.32 eV can be indexed to bridging S₂²⁻ and apical S²⁻ of MoS₂ whereas the peaks at 162.01 and 163.11 eV can be attributed to terminal S₂²⁻ of MoS₂ (Fig. 3b, f). In C 1s spectra of MoS₂/IPC-2 (Fig. S3b), peak located at 286.7 eV, assigned to C–O bonding, was also found [50]. The O 1s spectra can be de-convoluted to three peaks at 530.9, 531.9 and 533 eV (Fig. S3c). The existence of MoO_{3-x} or molybdenum oxysulfide species was also verified in Raman spectra of MoS₂/IPC-2. In Fig. 2b, the Raman spectra of both MoS₂/IPC-2 and bare MoS₂ exhibit B_{2g} and B_{1g} vibration modes of Mo–O bonds. In addition to vibration modes of Mo–O bonds, characteristic modes (in-plane Mo–S phonon mode (E_{2g}), out-of-plane Mo–S mode (A_{1g}) of MoS₂ were found which verifies existence of molybdenum sulfide species [51,52].

IPC with large amount of micropores and large specific surface area (SSA) were utilized as supporting material. Since few-layered MoS₂ are grown on the surface of IPC, decrease in SSA was expected. In this study, the pore structures of samples were measured by a Brauner-Emmett-Teller (BET) nitrogen adsorption/desorption method. As in Fig. 4a, the nitrogen sorption isotherms of IPC can be categorized as of typical type I, meaning that the pores were mainly composed of micropores. Compared to IPC, MoS₂/IPC-2 displayed widen knee of the isotherm, which indicates that the micropore quantity decreased as the MoS₂ is deposited on the carbon surface [45]. The SSA and pore volume of IPC was 1723 m² g⁻¹ and 0.91 cm³ g⁻¹, respectively. After

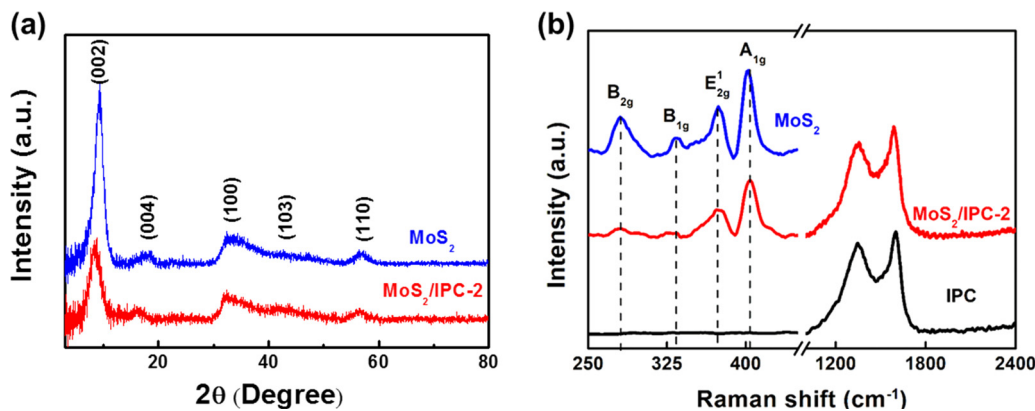


Fig. 2. (a) XRD patterns of bare MoS₂ and MoS₂/IPC-2 and (b) Raman spectra of bare MoS₂, MoS₂/IPC-2 and IPC.

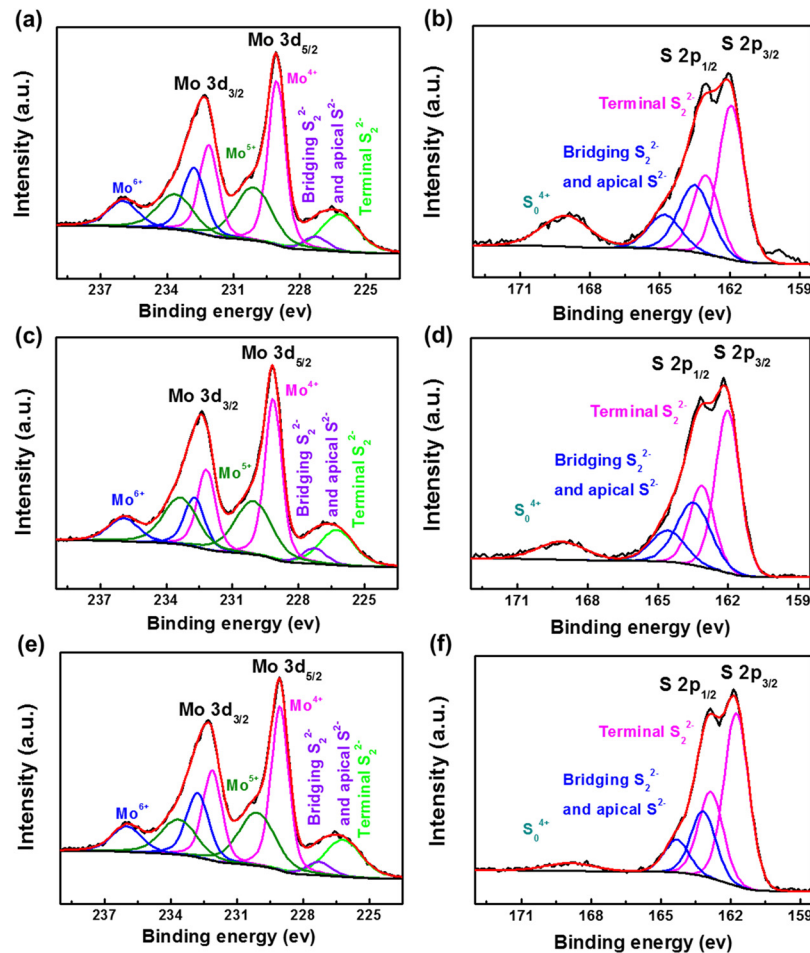


Fig. 3. High-resolution Mo 3d and S 2p spectrum for (a, b) MoS₂/IPC-1, (c, d) MoS₂/IPC-2, and (e, f) MoS₂/IPC-4.

deposition of MoS₂ on IPC surface, the SSA and pore volume became $616 \text{ m}^2 \text{ g}^{-1}$ and $0.43 \text{ cm}^3 \text{ g}^{-1}$, respectively. This was confirmed by analyzing pore size distribution (Fig. 4b) determined by the density function theory (DFT) method. Pore size distribution graph clearly reveals that the micropore volume (V_{micro}) is decreased and volume portion of meso/macropore ($V_{\text{meso/macro}}$) increased after deposition of MoS₂ on IPC. To note, significant decrease in V_{micro} to $V_{\text{meso/macro}}$ ratio of IPC was observed, which implies that large portion of micropore is occupied by the growth of MoS₂ on its surface. The BET SSA and pore volume of composites are summarized in Fig. 4c, d and Table S2.

Pore structure of bare MoS₂, IPC and MoS₂/IPC-2 were also characterized by SAXS (Fig. S5a). It has been reported that peaks from

$q = 3.14 \text{ nm}^{-1}$ (d-spacing of 2 nm) to $q = 6.4 \text{ nm}^{-1}$ (d-spacing of 0.98 nm) is the micropore range [53]. In this range, IPC has the highest scattering intensity followed by MoS₂/IPC-2 and bare MoS₂. Decreased scattering intensity after deposition of MoS₂ on IPC indicates that large portion of micropores is decreased which is consistent to the nitrogen adsorption observations. Unlike IPC and MoS₂/IPC-2, bare MoS₂ displayed lowest scattering intensity in the micropore range. This result indicates that bare MoS₂ does not have any micropores.

From the nitrogen adsorption analysis and SAXS, significant decrease in both specific surface area and micropore volume was observed. Since the morphology of IPC did not change after growth of MoS₂ nanosheets on its surface, significant decrease in micropore

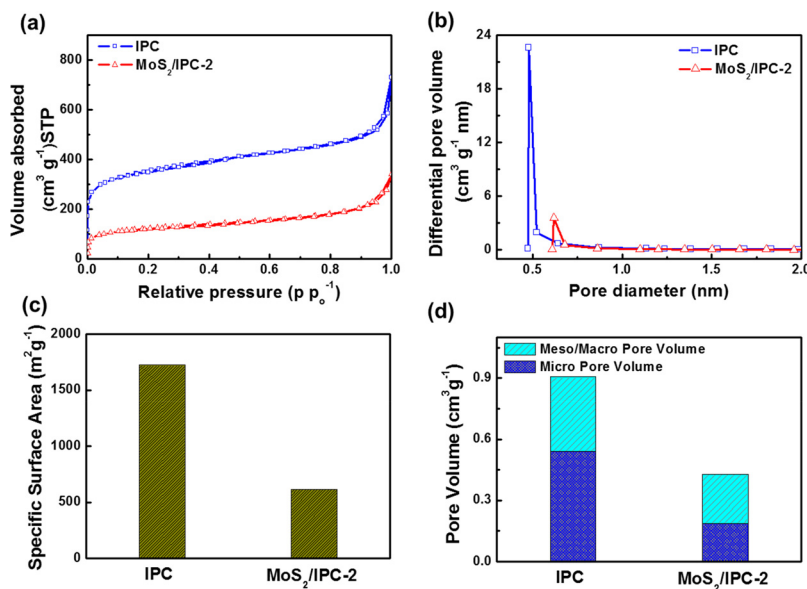


Fig. 4. (a) Nitrogen adsorption-desorption isotherms for IPC and MoS₂/IPC-2; (b) Pore size distribution curves for IPC and MoS₂/IPC-2; (c) Specific surface area and (d) pore volume for IPC and MoS₂/IPC-2.

volume can be understood as an evidence that deposited MoS₂ occupied the micropores and micropores served as nucleation sites for MoS₂ nanosheets. Research conducted by Liao et al. [54] and Liu et al. [40] also had shown that the edges of micropores on carbon surface can be used as a template to prepare nanostructured MoS₂.

IPC with different loading amount of MoS₂ nanosheets was prepared with same procedure by tuning the weight ratio of IPC/MoS₂ precursor from 1:1, 1:2, to 1:4. We designate the various MoS₂/IPC composite as “MoS₂/IPC-x”, whereas x refers to weight ratio of IPC to MoS₂

precursor. Fig. 5 shows the corresponding morphology of the prepared MoS₂/IPC composites. As shown in Fig. 5a, b, presence of IPC can be seen in both MoS₂/IPC-1 and MoS₂/IPC-4. In contrast, MoS₂/IPC-4, aggregated MoS₂ nanosheets forming nanoflower is observed. TEM image of MoS₂/IPC-4 (Fig. 5d) reveals that these nanoflowers are comprised of ~5 layers of MoS₂ nanosheets. Unlike MoS₂/IPC-4, few-layered MoS₂ grown on carbon surface is observed in MoS₂/IPC-1 (Fig. 5c). However, compared to TEM image of MoS₂/IPC-4 above, much lower density of the few-layered MoS₂ nanosheets is observed in

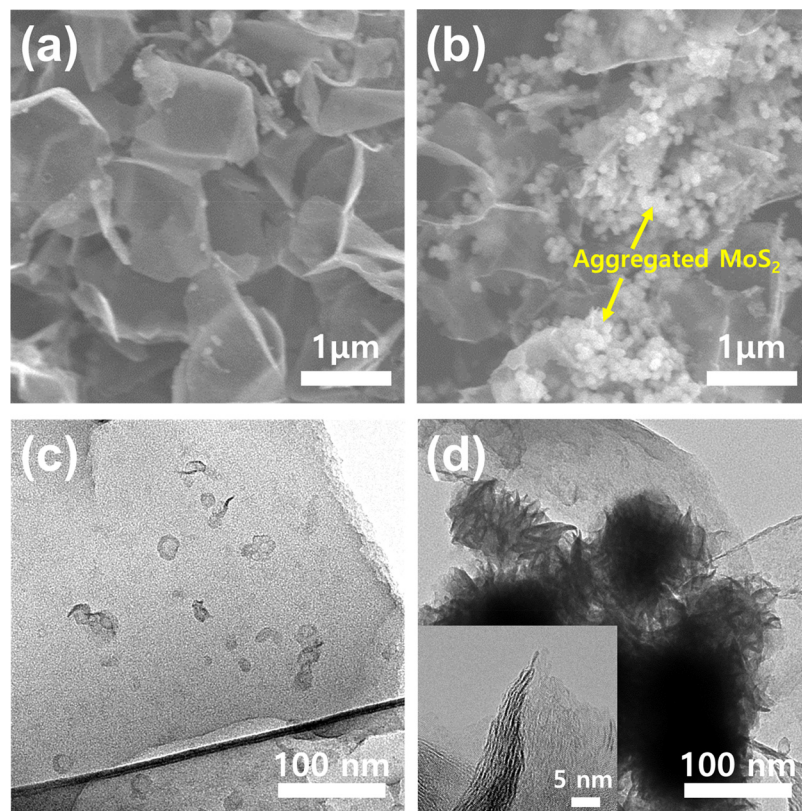


Fig. 5. SEM and TEM images of (a, c) MoS₂/IPC-1 and (b, d) MoS₂/IPC-4.

MoS₂/IPC-1.

X-ray fluorescence spectroscopy (XRF) was used to determine the mass loading and composition of MoS₂ deposited on the carbon support (**Table S1**). According to XRF analysis, weight percentage of MoS₂ in the composites increases as the amount of MoS₂ precursor increases. Meanwhile, atomic ratio of determined by the XRF analysis shows that loaded MoS₂ on all MoS₂/IPC composites was sulfur deficient which supports the existence of MoO_{3-x} or molybdenum oxysulfide [49,55]. Interestingly, as the amount of MoS₂ precursor increased, MoS₂ in the MoS₂/IPC composites became less sulfur deficient. Unlike MoS₂/IPC composites, bare MoS₂ showed S/Mo atomic ratio of 2.09. In previous reports, small sized MoS₂ nanosheets have been reported to be more susceptible to oxidation than bulk MoS₂ [56–59]. Decreased S/Mo atomic ratio upon decreasing amount of MoS₂ precursor further supports that MoS₂ formed on MoS₂/IPC composites exhibits much smaller dimension than bare MoS₂.

The detailed oxidation state of Mo species in bare MoS₂ and MoS₂/IPC composites was further studied by comparing relative percentages of Mo⁴⁺: Mo⁵⁺: Mo⁶⁺ in Mo 3d region of XPS [60]. For MoS₂/IPC-1, relative ratios from the XPS intensities was 26.98:53.54:19.48 at. %, confirming that significant proportion of Mo species is oxidized (**Table S2**). Moreover, oxidized sulfur species was verified in S2p spectra of MoS₂/IPC composites (**Fig. 3b, d, f**). Unlike MoS₂/IPC-1, relative percentages of Mo⁴⁺: Mo⁵⁺: Mo⁶⁺ of bare MoS₂ was 44.49:51.29:4.22. Upon increasing MoS₂ loading from MoS₂/IPC-2 to MoS₂/IPC-4, it is clearly observed that the portion of Mo⁶⁺ in Mo 3d spectra is significantly decreased which can be attributed to increased size of MoS₂, which is consistent to SEM results above. Meanwhile, it is interesting to note that large fraction of Mo species in MoS₂/IPC-2 is composed of Mo⁵⁺ species. Since the conductivity of molybdenum sulfide is related to oxidation state of Mo, large fraction of Mo⁵⁺ species implies that MoS₂ in MoS₂/IPC-2 composite is expected to exhibit high electron conductivity. Compared to MoO₃, oxygen deficient MoO_{3-x} has been reported to show several orders of magnitudes increase in conductivity [61,62].

In previous reports [63], it was found that the ratio between terminal S₂²⁻ and bridging S₂²⁻/apical S²⁻ is highly dependent on the size of MoS₂ nanosheets. A higher ratio of terminal S₂²⁻ to bridging S₂²⁻/apical S²⁻ indicates smaller size of MoS₂. For MoS₂/IPC composites, the ratio of terminal S₂²⁻ to bridging S₂²⁻/apical S²⁻ decreased accordingly as the amount of the MoS₂ precursor increased (**Fig. 3b, d, f**), (MoS₂/IPC-1: 3.04, MoS₂/IPC-2: 2.37, MoS₂/IPC-4: 2.08). However, as observed from TEM images above, the density of the few layered MoS₂ decreased by decreasing the amount of precursor.

3.2. Electrocatalytic properties of MoS₂/IPC composite

Catalytic activity of the synthesized MoS₂/IPC composites measured in an N₂-purged 0.5 M H₂SO₄ electrolyte using standard three-electrode measurements by depositing the electrocatalyst on a glassy carbon electrode (GCE). The optimum catalyst loading on the glassy carbon electrode was 0.254 mg cm⁻² (**Fig. S6**). We used Pt wire (0.5 mm diameter) as a reference because it exhibits the highest catalytic activity of any known material.

The polarization curves of MoS₂/IPC-1, MoS₂/IPC-2, MoS₂/IPC-4, IPC and bare MoS₂ normalized by area of the electrode shown on **Fig. 6a**. As expected, Pt wire showed excellent HER activity with a nearly zero overpotential whereas IPC showed negligible HER activity. Every MoS₂ containing samples exhibited high catalytic activity; MoS₂/IPC-2 shows the best catalytic activity with a high current density of 225 mA cm⁻² at an overpotential of 250 mV. In contrast, MoS₂ containing samples synthesized under different conditions (i.e. MoS₂/IPC-1, MoS₂/IPC-4, and bare MoS₂) showed lower current densities (i.e. 84 mA cm⁻², 83 mA cm⁻², and 15 mA cm⁻², respectively) at overpotentials of 250 mV (**Fig. 6a, c, Table S5**). Large differences in catalytic activity between bare MoS₂ and MoS₂/IPC composites indicate

that IPC could increase electron transportation to active sites existing at the edges of nanosheets. The differences in catalytic activities among the MoS₂/IPC composites may be ascribed to differences in number of exposed active edges formed according to different weight ratios of MoS₂ precursor IPC. To compare the intrinsic catalytic activity of MoS₂/IPC composites, the MoS₂ mass activity of the above catalysts were calculated. **Fig. S11** compares the mass-normalized HER performances of MoS₂/IPC composites. At overpotential of 200 mV, MoS₂/IPC-2 exhibits highest catalytic current of 400 mA mg⁻¹ followed by 185 mA mg⁻¹ of MoS₂/IPC-1 and 115 mA mg⁻¹ of MoS₂/IPC-4, demonstrating that the intrinsic catalytic activity of MoS₂/IPC-2 is much higher than that of MoS₂/IPC-4 and MoS₂/IPC-1. The catalytic activity of MoS₂/IPC-2 normalize by the MoS₂ mass surpasses most of the MoS₂/carbon electrocatalysts enlisted in **Table S5** which indicates that few-layered MoS₂ deposited on IPC exhibits high intrinsic catalytic activity despite its oxidized state.

To further study the detailed HER kinetics of MoS₂/IPC composites and bare MoS₂, Tafel plots were constructed by converting the polarization curves to graphs of the logarithm of the cathodic current versus the overpotential (**Fig. 6b**). The Tafel plots were analyzed by fitting the Tafel equation to the linear regions. The Tafel equation is:

$$\eta = b \log(j) + a \quad (1)$$

where *a* is the exchange current and *b* is the Tafel slope. The Tafel slope is a parameter that can diagnose HER mechanisms occurring at the surface of the electrocatalyst. For MoS₂, wide range of Tafel slopes has been reported. The primary reason for this is that Tafel slope is largely dependent on electrical conductivity, crystallinity of the MoS₂ and surface area of the catalyst. The obtained Tafel slopes for bare MoS₂, MoS₂/IPC-1, MoS₂/IPC-2, and MoS₂/IPC-4 were 64, 40, 38, and 43 mV dec⁻¹ respectively (**Fig. 6c**). All MoS₂/IPC composites exhibited similar low Tafel slopes near 40 mV dec⁻¹, which suggests that the Volmer-Heyrovsky reaction mechanism is occurring on the MoS₂/IPC composites [17]. Work done by Li et al. [64] demonstrated that the terminal disulfide groups at the edges of the low crystalline MoS₂ are responsible for low Tafel slope. The slight differences in Tafel slope among the MoS₂/IPC composites may ascribed to differences in electrical conductivity and surface area of the catalyst [65,66].

The electrochemical surface area (ECSA) was estimated by measuring the double layered capacitance (*C_d*) in non-Faradaic potential region (**Fig. 6d**, **Fig. S7**). Since very significant area of carbon support is not covered by MoS₂, the capacitance values cannot be directly correlated to the number of active sites [67]. However, measured capacitance values may be used to roughly estimate the total surface of the catalyst modified electrode. MoS₂/IPC-1 had the highest capacitance value of 16.67 mF cm⁻² followed by MoS₂/IPC-2 at 16.22 mF cm⁻², MoS₂/IPC-4 at 11.48 mF cm⁻², and bare MoS₂ at 4.60 mF cm⁻². MoS₂/IPC-4 showed lowest capacitance value due to presence of large numbers of aggregated multilayered MoS₂ on its surface. Despite the highest capacitance value, MoS₂/IPC-1 exhibited lowest catalytic current density. This may be resulted by decreased mass transportation for high surface area catalyst lacking electrocatalytically active sites [65].

The electrochemical impedance spectroscopy (EIS) measurements were conducted to characterize the interface reactions and kinetics of HER. **Fig. 7a** shows Nyquist plots of bare MoS₂ and MoS₂/IPC composites. The Nyquist plot was fitted to a corresponding equivalent circuit of two CPE (constant phase element) model, which consist of electrolyte resistance in series with two parallel R-CPE elements (**Fig. S10**). For two CPE model, high-frequency semicircle is related to the surface porosity whereas the low frequency is related to the charge transfer process. Two CPE model is composed of following circuit elements: *R*_s is attributed to the solution resistance, CPE is related to the double-layer capacity of the electrodes, *R_c* and charge transfer resistance (*R_{ct}*) are related to the porous structure and the reaction kinetics of the HER, respectively. MoS₂/IPC-2 had the smallest *R_{ct}* of 10.14 Ω compared to 16.75 Ω for MoS₂/IPC-1, 14.70 Ω for MoS₂/IPC-4 and 43.74 Ω for bare

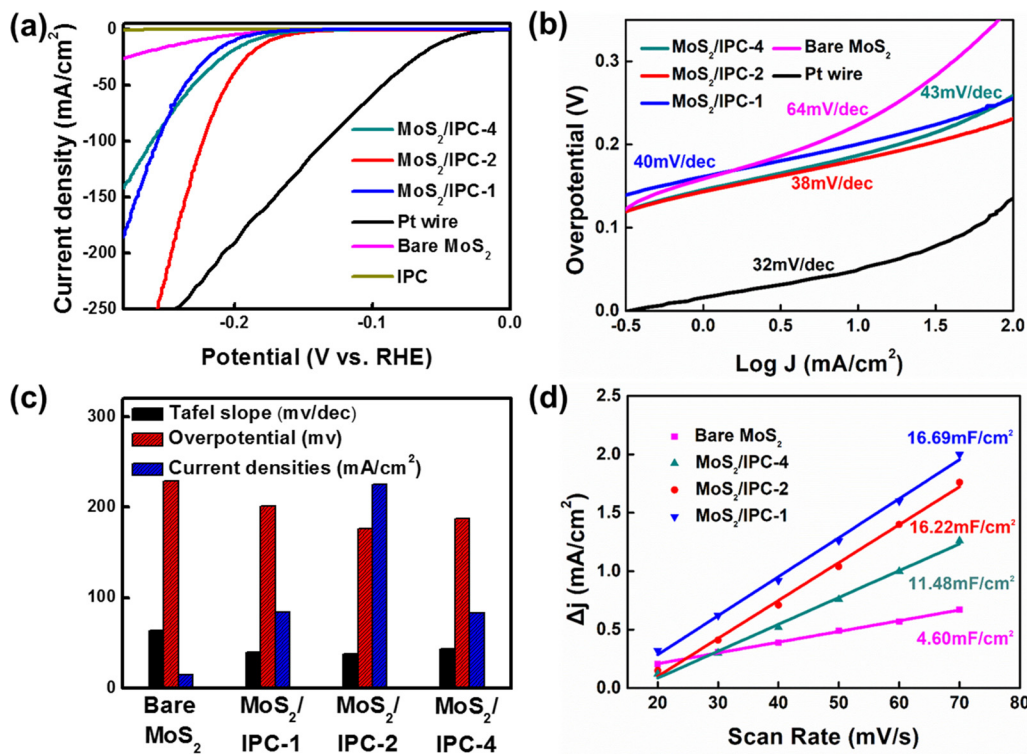


Fig. 6. (a) HER polarization curves and (b) Tafel plot of corresponding catalyst of bare MoS₂, MoS₂/IPC composites, IPC and Pt wire; (c) Comparison of Tafel slope (black), overpotential (red) at 10 mA cm^{-2} , and current density (blue) at overpotential 250 mV of bare MoS₂ and MoS₂/IPC composites; (d) Summary of ECSA by measuring cyclic voltammetry measurements for bare MoS₂ and MoS₂/IPC composites (For interpretation of the references to colour in this figure legend, the reader is referred to the web version of this article).

MoS₂ (Fig. 7a, Table S4). MoS₂/IPC composites exhibit lower R_{ct} than bare MoS₂, which can be attributed to IPC acting as conductive support in the composites. From the following result, we verified that MoS₂/IPC-2 is the optimum electrocatalyst having the least R_{ct} from catalyst to reactants. It is important to note that MoS₂/IPC-4 exhibits lower R_{ct} than MoS₂/IPC-1. This difference in R_{ct} between MoS₂/IPC-1 and

MoS₂/IPC-4 may arise from low density of few-layered MoS₂ and high surface area of MoS₂/IPC-1 forming thick film on current collector as we explained from ECSA results.

To assess the long term stability of MoS₂/IPC-2, cyclic voltammetry scans (1000 cycles) and constant current input (-10 mA cm^{-2} , -50 mA cm^{-2}) was held. MoS₂/IPC-2 exhibits negligible catalytic loss

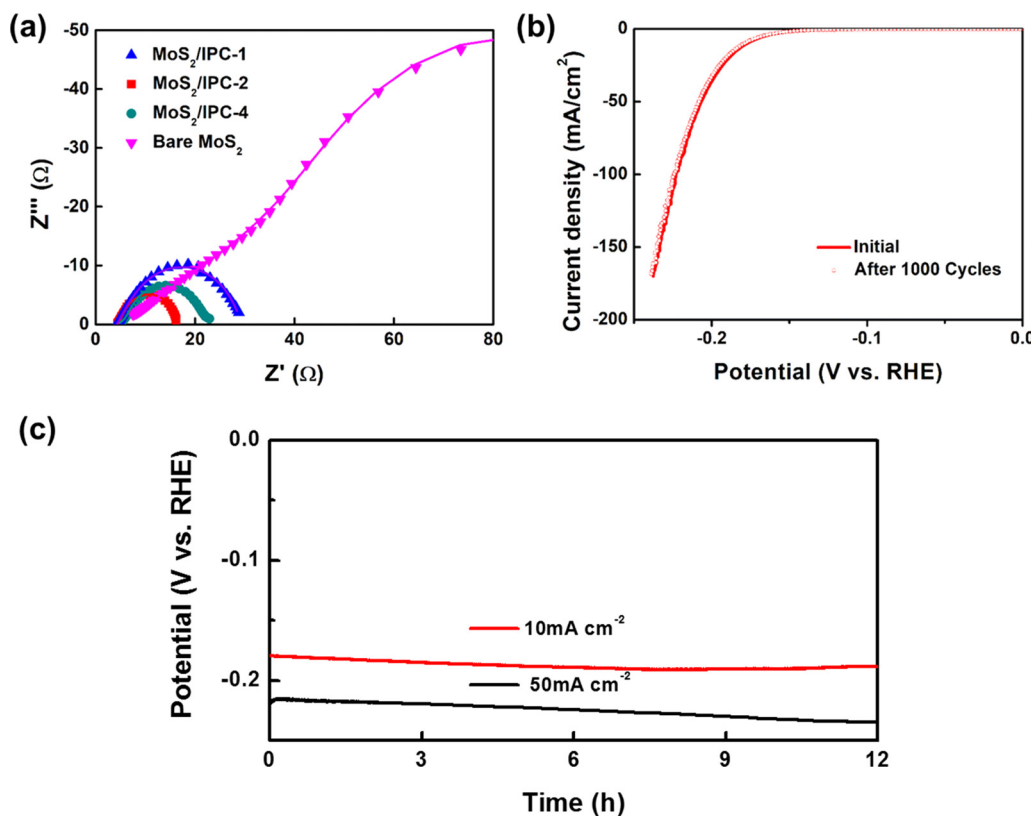


Fig. 7. (a) Nyquist plots of bare MoS₂ and MoS₂/IPC composites; (b) Polarization curves of MoS₂/IPC-2 before and after 1000th cycle; (c) Galvanostatic cycle stability test on MoS₂/IPC-2 under current density of -10 mA cm^{-2} and -50 mA cm^{-2} .

even after 1000 cyclic voltammetry (CV) cycles between -0.3 V and 0.2 V vs. RHE at a scan rate of 50 mV s⁻¹ (Fig. 7b). The long-term stability of MoS₂/IPC-2 was assessed through the chronopotentiometry test under constant current input of -10 mA cm⁻² and -50 mA cm⁻² (Fig. 7c). At -50 mA cm⁻², MoS₂/IPC-2 exhibited a constant curve with a ~ 20 mV increase in the overpotential after 12 h whereas chronopotentiometry test held at -10 mA cm⁻² shows negligible increase in overpotential. This implies that the MoS₂/IPC-2 exhibits good electrochemical stability during HER.

In comparison with the catalytic activity of MoS₂/IPC composites by means of different indicators, we found that MoS₂/IPC-2 had the most optimal catalytic performance. Although MoS₂/IPC-1 had the smallest MoS₂ which was supported by highest ratio of terminal S₂²⁻ to bridging S₂²⁻/apical S²⁻ and TEM results, low density of few-layered MoS₂ may result in lowest catalytic activity among the MoS₂/IPC composites. Moreover, significant portion of Mo species in MoS₂/IPC-1 was oxidized which has been reported to be detrimental for HER performance [68]. For MoS₂/IPC-4, despite the large portion of unoxidized Mo species, amount of aggregated MoS₂ increased which causes difficulties to expose its catalytically active edges.

The excellent electrochemical HER catalytic performance of optimized MoS₂/IPC composite (MoS₂/IPC-2) can be attributed to three factors: (1) High density of few-layered MoS₂ nanosheets expose a significant amount of catalytically active edges. (2) The optimized morphology of MoS₂/IPC-2 composite facilitates mass transport and electrical conductance. (3) Reduced sizes of MoS₂ nanosheets decreases charge transfer resistance which leads an increased in catalytic activity. Conclusively, MoS₂/IPC-2 as a low-cost and high-performance catalyst shows promise for use in HER electrocatalysts in practical applications.

4. Conclusion

In summary, a composite material consisting of few-layered MoS₂ supported on 3D interconnected porous carbon was developed as an efficient HER electrocatalyst. The formation of few-layered MoS₂ may be ascribed to micropores on IPC surface acting as nucleation sites. Overall, due to the high density few-layered MoS₂ with less aggregation, the optimized catalyst MoS₂/IPC-2 exhibited high HER activity with a large cathodic current density (225 mA cm⁻² at 250 mV), small Tafel slope of 38 mV dec⁻¹ and long-term durability. The synthesis in this work presents an overall cost-effective approach to produce high density few-layered MoS₂ on a conductive support; consequently, this synthetic approach can also be extended to other applications that require few-layered MoS₂.

Acknowledgments

This research is supported by the Basic Science Research Program through the National Research Foundation of Korea (NRF) funded by the Ministry of Education (NRF-2015R1D1A1A01060398) and by the Center of Integrated Smart Sensors funded by the Ministry of Science, ICT and Future Planning, Republic of Korea, as Global Frontier Project (CISI- 012M3A6A6054186). The authors also acknowledge the supports of the National Natural Science Foundation of China (Grant no. 21703200), the Natural Science Foundation of Jiangsu Province (Grant no. BK20170485), the Natural Science Foundation of the Jiangsu Higher Education Institutions of China (Grant no. 17KJB150043), and the Priority Academic Program Development of Jiangsu Higher Education Institutions.

Appendix A. Supplementary data

Supplementary material related to this article can be found, in the online version, at doi:<https://doi.org/10.1016/j.apcatb.2019.02.035>.

References

- [1] M.S. Dresselhaus, I.L. Thomas, Alternative energy technologies, *Nature* 414 (2001) 332–337.
- [2] J.A. Turner, Sustainable hydrogen production, *Science* 305 (2004) 972.
- [3] P. Lianos, Review of recent trends in photoelectrocatalytic conversion of solar energy to electricity and hydrogen, *Appl. Catal. B-Environ.* 210 (2017) 235–254.
- [4] D.S. Kong, J.J. Cha, H.T. Wang, H.R. Lee, Y. Cui, First-row transition metal dichalcogenide catalysts for hydrogen evolution reaction, *Synth. Lect. Energy Environ. Technol. Sci. Soc.* 6 (2013) 3553–3558.
- [5] Y. Zheng, Y. Jiao, Y.H. Zhu, L.H. Li, Y. Han, Y. Chen, A.J. Du, M. Jaroniec, S.Z. Qiao, Hydrogen evolution by a metal-free electrocatalyst, *Nat. Commun.* 5 (2014).
- [6] Z.W. Chen, D. Higgins, A.P. Yu, L. Zhang, J.J. Zhang, A review on non-precious metal electrocatalysts for PEM fuel cells, *Synth. Lect. Energy Environ. Technol. Sci. Soc.* 4 (2011) 3167–3192.
- [7] J. Deng, P.J. Ren, D.H. Deng, L. Yu, F. Yang, X.H. Bao, Highly active and durable non-precious-metal catalysts encapsulated in carbon nanotubes for hydrogen evolution reaction, *Synth. Lect. Energy Environ. Technol. Sci. Soc.* 7 (2014) 1919–1923.
- [8] Y.J. Ko, J.M. Cho, I. Kim, D.S. Jeong, K.S. Lee, J.K. Park, Y.J. Baik, H.J. Choi, W.S. Lee, Tungsten carbide nanowalls as electrocatalyst for hydrogen evolution reaction: New approach to durability issue, *Appl. Catal. B-Environ.* 203 (2017) 684–691.
- [9] S.-K. Park, J.K. Kim, Y. Chan Kang, Metal-organic framework-derived CoSe₂/(NiCo)Se₂ box-in-box hollow nanocubes with enhanced electrochemical properties for sodium-ion storage and hydrogen evolution, *J. Mater. Chem. A Mater. Energy Sustain.* 5 (2017) 18823–18830.
- [10] J.K. Kim, G.D. Park, J.H. Kim, S.K. Park, Y.C. Kang, Rational design and synthesis of extremely efficient macroporous CoSe₂-CNT composite microspheres for hydrogen evolution reaction, *Small* 13 (2017).
- [11] Z. Mo, H. Xu, Z. Chen, X. She, Y. Song, J. Lian, X. Zhu, P. Yan, Y. Lei, S. Yuan, H. Li, Construction of MnO₂/Monolayer g-C₃N₄ with Mn vacancies for Z-scheme overall water splitting, *Appl. Catal. B* 241 (2019) 452–460.
- [12] A.B. Laursen, S. Kegnæs, S. Dahl, I. Chorkendorff, Molybdenum sulfides-efficient and viable materials for electro- and photoelectrocatalytic hydrogen evolution, *Synth. Lect. Energy Environ. Technol. Sci. Soc.* 5 (2012) 5577–5591.
- [13] M. Ledendecker, J.S. Mondschein, O. Kasian, S. Geiger, D. Gohl, M. Schalenbach, A. Zeradjanin, S. Cherevko, R.E. Schaak, K. Mayrhofer, Stability and activity of non-noble-metal-based catalysts toward the hydrogen evolution reaction, *Angew. Chem. Int. Ed.* 56 (2017) 9767–9771.
- [14] B. Hinnemann, P.G. Moses, J. Bonde, K.P. Jorgensen, J.H. Nielsen, S. Horch, I. Chorkendorff, J.K. Norskov, Biomimetic hydrogen evolution: MoS₂ nanoparticles as catalyst for hydrogen evolution, *J. Am. Chem. Soc.* 127 (2005) 5308–5309.
- [15] J. Liu, Y. Liu, D. Xu, Y. Zhu, W. Peng, Y. Li, F. Zhang, X. Fan, Hierarchical “nanoroll” like MoS₂/Ti₃C₂T_x hybrid with high electrocatalytic hydrogen evolution activity, *Appl. Catal. B-Environ.* 55 (2019) 2078–2081.
- [16] Y.Z. Liu, H.Y. Zhang, J. Ke, J.Q. Zhang, W.J. Tian, X.Y. Xu, X.G. Duan, H.Q. Sun, M.O. Tade, S.B. Wang, OD (MoS₂)/2D (g-C₃N₄) heterojunctions in Z-scheme for enhanced photocatalytic and electrochemical hydrogen evolution, *Appl. Catal. B-Environ.* 228 (2018) 64–74.
- [17] K. Zhang, B. Jin, Y. Gao, S. Zhang, H. Shin, H. Zeng, J.H. Park, Aligned hetero-interface-induced 1T-MoS₂ monolayer with near-ideal gibbs free for stable hydrogen evolution reaction, *Small* (2019) 1804903.
- [18] H.I. Karunadasa, E. Montalvo, Y.J. Sun, M. Majda, J.R. Long, C.J. Chang, A molecular MoS₂ edge site mimic for catalytic hydrogen generation, *Science* 335 (2012) 698–702.
- [19] J. Liu, Y. Liu, D. Xu, Y. Zhu, W. Peng, Y. Li, F. Zhang, X. Fan, Hierarchical “nanoroll” like MoS₂/Ti₃C₂T_x hybrid with high electrocatalytic hydrogen evolution activity, *Appl. Catal. B* 241 (2019) 89–94.
- [20] Y. Li, K. Yin, L. Wang, X. Lu, Y. Zhang, Y. Liu, D. Yan, Y. Song, S. Luo, Engineering MoS₂nanomesh with holes and lattice defects for highly active hydrogen evolution reaction, *Appl. Catal. B* 239 (2018) 537–544.
- [21] T.F. Jaramillo, K.P. Jorgensen, J. Bonde, J.H. Nielsen, S. Horch, I. Chorkendorff, Identification of active edge sites for electrochemical H₂ evolution from MoS₂ nanocatalysts, *Science* 317 (2007) 100–102.
- [22] Z.Z. Wu, B.Z. Fang, Z.P. Wang, C.L. Wang, Z.H. Liu, F.Y. Liu, W. Wang, A. Alfantazi, D.Z. Wang, D.P. Wilkinson, MoS₂nanosheets: a designed structure with high active site density for the hydrogen evolution reaction, *ACS Catal.* 3 (2013) 2101–2107.
- [23] A. Bruix, H.G. Fuchtbauer, A.K. Tuxen, A.S. Walton, M. Andersen, S. Porsgaard, F. Besenbacher, B. Hammer, J.V. Lauritsen, In situ detection of active edge sites in single-layer MoS₂ catalysts, *ACS Nano* 9 (2015) 9322–9330.
- [24] M.V. Bollinger, J.V. Lauritsen, K.W. Jacobsen, J.K. Norskov, S. Helveg, F. Besenbacher, One-dimensional metallic edge states in MoS₂, *Phys. Rev. Lett.* 87 (2001) 196803.
- [25] Y. Yu, S.Y. Huang, Y. Li, S.N. Steinmann, W. Yang, L. Cao, Layer-dependent electrocatalysis of MoS₂ for hydrogen evolution, *Nano Lett.* 14 (2014) 553–558.
- [26] W.Y. Sun, P. Li, X. Liu, J.J. Shi, H.M. Sun, Z.L. Tao, F.J. Li, J. Chen, Size-controlled MoS₂ nanodots supported on reduced graphene oxide for hydrogen evolution reaction and sodium-ion batteries, *Nano Res.* 10 (2017) 2210–2222.
- [27] K. Chang, H. Pang, X. Hai, G. Zhao, H. Zhang, L. Shi, F. Ichihara, J. Ye, Ultra-small freestanding amorphous molybdenum sulfide colloidal nanodots for highly efficient photocatalytic hydrogen evolution reaction, *Appl. Catal. B-Environ.* 232 (2018) 446–453.
- [28] F. Li, J. Li, Z. Cao, X. Lin, X. Li, Y. Fang, X. An, Y. Fu, J. Jin, R. Li, MoS₂quantum dot decorated RGO: a designed electrocatalyst with high active site density for the

hydrogen evolution reaction, *J. Mater. Chem. A Mater. Energy Sustain.* 3 (2015) 21772–21778.

[29] X. Ren, L. Pang, Y. Zhang, X. Ren, H. Fan, S. Liu, One-step hydrothermal synthesis of monolayer MoS₂ quantum dots for highly efficient electrocatalytic hydrogen evolution, *J. Mater. Chem. A Mater. Energy Sustain.* 3 (2015) 10693–10697.

[30] D. Gopalakrishnan, D. Damien, M.M. Shaijumon, MoS₂ quantum dot-interspersed exfoliated MoS₂ nanosheets, *ACS Nano* 8 (2014) 5297–5303.

[31] S.K. Park, D.Y. Chung, D. Ko, Y.E. Sung, Y. Piao, Three-dimensional carbon foam/N-doped graphene@MoS₂ hybrid nanostructures as effective electrocatalysts for the hydrogen evolution reaction, *J. Mater. Chem. A Mater. Energy Sustain.* 4 (2016) 12720–12725.

[32] M. Chatti, T. Gengenbach, R. King, L. Spiccia, A.N. Simonov, Vertically aligned interlayer expanded MoS₂ nanosheets on a carbon support for hydrogen evolution electrocatalysis, *Chem. Mater.* 29 (2017) 3092–3099.

[33] Y. Sun, F. Alimohammadi, D. Zhang, G. Guo, Enabling colloidal synthesis of edge-oriented MoS₂ with expanded interlayer spacing for enhanced HER catalysis, *Nano Lett.* 17 (2017) 1963–1969.

[34] Y. Yan, B. Xia, N. Li, Z. Xu, A. Fisher, X. Wang, Vertically oriented MoS₂ and WS₂ nanosheets directly grown on carbon cloth as efficient and stable 3-dimensional hydrogen-evolving cathodes, *J. Mater. Chem. A Mater. Energy Sustain.* 3 (2015) 131–135.

[35] D. Kong, H. Wang, J.J. Cha, M. Pasta, K.J. Koski, J. Yao, Y. Cui, Synthesis of MoS₂ and MoSe₂ films with vertically aligned layers, *Nano Lett.* 13 (2013) 1341–1347.

[36] H. Wang, Z. Lu, S. Xu, D. Kong, J.J. Cha, G. Zheng, P.C. Hsu, K. Yan, D. Bradshaw, F.B. Prinz, Y. Cui, Electrochemical tuning of vertically aligned MoS₂ nanofilms and its application in improving hydrogen evolution reaction, *Proc. Natl. Acad. Sci.* 110 (2013) 19701–19706.

[37] F. Gloaguen, J.M. Leger, C. Lamy, Electrocatalytic oxidation of methanol on platinum nanoparticles electrodeposited onto porous carbon substrates, *J. Appl. Electrochem.* 27 (1997) 1052–1060.

[38] J. Ying, G.P. Jiang, Z.P. Cano, L. Han, X.Y. Yang, Z.W. Chen, Nitrogen-doped hollow porous carbon polyhedrons embedded with highly dispersed Pt nanoparticles as a highly efficient and stable hydrogen evolution electrocatalyst, *Nano Energy* 40 (2017) 88–94.

[39] H.B. Zhang, P.F. An, W. Zhou, B.Y. Guan, P. Zhang, J.C. Dong, X.W. Lou, Dynamic traction of lattice-confined platinum atoms into mesoporous carbon matrix for hydrogen evolution reaction, *Sci. Adv.* 4 (2018).

[40] L.B. Huang, L. Zhao, Y. Zhang, Y.Y. Chen, Q.H. Zhang, H. Luo, X. Zhang, T. Tang, L. Gu, J.S. Hu, Self-limited on-site conversion of MoO₃ nanodots into vertically aligned ultrasmall monolayer MoS₂ for efficient hydrogen evolution, *Adv. Energy Mater.* (2018) 1800734.

[41] L. Liao, J. Zhu, X.J. Bian, L.N. Zhu, M.D. Scanlon, H.H. Girault, B.H. Liu, MoS₂ formed on mesoporous graphene as a highly active catalyst for hydrogen evolution, *Adv. Funct. Mater.* 23 (2013) 5326–5333.

[42] Z. Hu, L. Wang, K. Zhang, J. Wang, F. Cheng, Z. Tao, J. Chen, MoS₂ nanoflowers with expanded interlayers as high-performance anodes for sodium-ion batteries, *Angew. Chem. Int. Ed.* 53 (2014) 12794–12798.

[43] S.Y. Cho, S.J. Kim, Y. Lee, J.S. Kim, W.B. Jung, H.W. Yoo, J. Kim, H.T. Jung, Highly enhanced gas adsorption properties in vertically aligned MoS₂ Layers, *ACS Nano* 9 (2015) 9314–9321.

[44] K. Ai, C. Ruan, M. Shen, L. Lu, MoS₂ nanosheets with widened interlayer spacing for high-efficiency removal of mercury in aquatic systems, *Adv. Funct. Mater.* 26 (2016) 5542–5549.

[45] M. Sevilla, A.B. Fuertes, Direct synthesis of highly porous interconnected carbon nanosheets and their application as high-performance supercapacitors, *ACS Nano* 8 (2014) 5069–5078.

[46] Y. Li, H. Wang, L. Xie, Y. Liang, G. Hong, H. Dai, MoS₂ nanoparticles grown on graphene: an advanced catalyst for the hydrogen evolution reaction, *J. Am. Chem. Soc.* 133 (2011) 7296–7299.

[47] J.X. Guo, F.F. Li, Y.F. Sun, X. Zhang, L. Tang, Oxygen-incorporated MoS₂ ultrathin nanosheets grown on graphene for efficient electrochemical hydrogen evolution, *J. Power Sources* 291 (2015) 195–200.

[48] L. Ma, J. Ye, W. Chen, J. Wang, R. Liu, J.Y. Lee, Synthesis of few-layer MoS₂-Graphene composites with superior electrochemical lithium-storage performance by an ionic-liquid-mediated hydrothermal route, *ChemElectroChem* 2 (2015) 538–546.

[49] B. Mohanty, M. Ghorbani-Asl, S. Kretschmer, A. Ghosh, P. Guha, S.K. Panda, B. Jena, A.V. Krasheninnikov, B.K. Jena, MoS₂ quantum dots as efficient catalyst materials for the oxygen evolution reaction, *ACS Catal.* 8 (2018) 1683–1689.

[50] Y. Liu, Y. Zhu, X. Fan, S. Wang, Y. Li, F. Zhang, G. Zhang, W. Peng, (OD/3D) MoS₂ on porous graphene as catalysts for enhanced electrochemical hydrogen evolution, *Carbon* 121 (2017) 163–169.

[51] A. Liu, L. Zhao, J. Zhang, L. Lin, H. Wu, Solvent-assisted oxygen incorporation of vertically aligned MoS₂ ultrathin nanosheets decorated on reduced graphene oxide for improved electrocatalytic hydrogen evolution, *ACS Appl. Mater. Interfaces* 8 (2016) 25210–25218.

[52] J. Xie, J. Zhang, S. Li, F. Grote, X. Zhang, H. Zhang, R. Wang, Y. Lei, B. Pan, Y. Xie, Controllable disorder engineering in oxygen-incorporated MoS₂ ultrathin nanosheets for efficient hydrogen evolution, *J. Am. Chem. Soc.* 135 (2013) 17881–17888.

[53] A. Petzold, A. Juhl, J. Scholz, B. Ufer, G. Goerigk, M. Fröba, M. Ballauff, S. Mascotto, Distribution of sulfur in Carbon/Sulfur nanocomposites analyzed by small-angle X-ray scattering, *Langmuir* 32 (2016) 2780–2786.

[54] Y. Liu, X. Zhou, T. Ding, C. Wang, Q. Yang, 3D architecture constructed via the confined growth of MoS₂ nanosheets in nanoporous carbon derived from metal-organic frameworks for efficient hydrogen production, *Nanoscale* 7 (2015) 18004–18009.

[55] D. Gopalakrishnan, D. Damien, B. Li, H. Gullappalli, V.K. Pillai, P.M. Ajayan, M.M. Shaijumon, Electrochemical synthesis of luminescent MoS₂ quantum dots, *Chem. Commun.* 51 (2015) 6293–6296.

[56] S. Xu, D. Li, P. Wu, One-Pot, facile, and versatile synthesis of monolayer MoS₂/WS₂ quantum dots as bioimaging probes and efficient electrocatalysts for hydrogen evolution reaction, *Adv. Funct. Mater.* 25 (2015) 1127–1136.

[57] J. Benson, M. Li, S. Wang, P. Wang, P. Papakonstantinou, Electrocatalytic hydrogen evolution reaction on edges of a few layer molybdenum disulfide nanodots, *ACS Appl. Mater. Interfaces* 7 (2015) 14113–14122.

[58] E.P. Nguyen, B.J. Carey, T. Daeneke, J.Z. Ou, K. Latham, S. Zhiuiykov, K. Kalantazadeh, Investigation of two-solvent grinding-assisted liquid phase exfoliation of layered MoS₂, *Chem. Mater.* 27 (2015) 53–59.

[59] X. Li, X. Lv, N. Li, J. Wu, Y.-Z. Zheng, X. Tao, One-step hydrothermal synthesis of high-percentage 1T-phase MoS₂ quantum dots for remarkably enhanced visible-light-driven photocatalytic H₂ evolution, *Appl. Catal. B* 243 (2019) 76–85.

[60] D. Escalera-López, Y. Niu, S.J. Park, M. Isaacs, K. Wilson, R.E. Palmer, N.V. Rees, Hydrogen evolution enhancement of ultra-low loading, size-selected molybdenum sulfide nanoclusters by sulfur enrichment, *Appl. Catal. B* 235 (2018) 84–91.

[61] B. Yang, Y. Chen, Y. Cui, D. Liu, B. Xu, J. Hou, Over 100-nm-thick MoO_x films with superior hole collection and transport properties for organic solar cells, *Adv. Energy Mater.* 8 (2018) 1800698.

[62] K. Crowley, G. Ye, R. He, K. Abbasi, X.P. Gao, α -MoO₃ as a conductive 2D oxide: tunable n-type electrical transport via oxygen vacancy and fluorine doping, *ACS Appl. Nano Mater.* 1 (2018) 6407–6413.

[63] H. Huang, J. Huang, W. Liu, Y. Fang, Y. Liu, Ultradispersed and single-layered MoS₂ nanoflakes strongly coupled with graphene: an optimized structure with high kinetics for the hydrogen evolution reaction, *ACS Appl. Mater. Interfaces* 9 (2017) 39380–39390.

[64] Y.P. Li, Y.F. Yu, Y.F. Huang, R.A. Nielsen, W.A. Goddard, Y. Li, L.Y. Cao, Engineering the composition and crystallinity of molybdenum sulfide for high-performance electrocatalytic hydrogen evolution, *ACS Catal.* 5 (2015) 448–455.

[65] J.D. Benck, Z.B. Chen, L.Y. Kuritzky, A.J. Forman, T.F. Jaramillo, Amorphous molybdenum sulfide catalysts for electrochemical hydrogen production: insights into the origin of their catalytic activity, *ACS Catal.* 2 (2012) 1916–1923.

[66] A.P. Murthy, J. Theerthagiri, J. Madhavan, K. Murugan, Highly active MoS₂/carbon electrocatalysts for the hydrogen evolution reaction-insight into the effect of the internal resistance and roughness factor on the Tafel slope, *Phys. Chem. Chem. Phys.* 19 (2017) 1988–1998.

[67] D.Y. Chung, J.M. Yoo, S. Park, G.Y. Jung, J.S. Kang, C.-Y. Ahn, S.K. Kwak, Y.-E. Sung, Edge-terminated MoS₂ nanoassembled electrocatalyst via in situ hybridization with 3D carbon network, *Small* 14 (2018) 1802191.

[68] Z. Chen, D. Cummins, B.N. Reinecke, E. Clark, M.K. Sunkara, T.F. Jaramillo, Core-shell MoO₃–MoS₂ nanowires for hydrogen evolution: a functional design for electrocatalytic materials, *Nano Lett.* 11 (2011) 4168–4175.